



Mesoporous implantable Pt/SrTiO₃:C,N nanocuboids delivering enhanced photocatalytic H₂-production activity via plasmon-induced interfacial electron transfer



Ioannis Tamiolakis^a, Dong Liu^b, Fang-Xing Xiao^b, Jian Xie^c, Ioannis T. Papadas^d, Teddy Salim^c, Bin Liu^b, Qichun Zhang^{c,e}, Stelios A. Choulis^d, Gerasimos S. Armatas^{a,*}

^a University of Crete, Department of Materials Science and Technology, Heraklion 71003, Greece

^b Nanyang Technological University, School of Chemical and Biomedical Engineering, 62 Nanyang Drive, Singapore 637459, Singapore

^c Nanyang Technological University, School of Materials Science and Engineering Singapore 639798, Singapore

^d Cyprus University of Technology, Department of Mechanical Engineering and Materials Science and Engineering, Limassol 3041, Cyprus

^e Nanyang Technological University, Division of Chemistry and Biological Chemistry, School of Physical and Mathematical Science, Singapore 637371, Singapore

ARTICLE INFO

Keywords:
Strontium titanate
Nanoparticles
Mesoporous materials
Hydrogen production
Photocatalysis

ABSTRACT

Band edge engineering of semiconductor nanostructures is one of the most appealing approaches to enhance light absorption, carrier separation and, ultimately, solar to fuel conversion efficiency. In this study, we devise a facile polymer-assisted sol-gel chemical method to prepare highly porous, crystalline implanted SrTiO₃ (STO) nanoparticles and demonstrate their performance for photocatalytic hydrogen generation from water. X-ray scattering, electron microscopy, and nitrogen physisorption data corroborate that the as-made catalysts comprise 100-nm-sized nanocuboid particles containing a highly internal porous structure (BET surface area $\sim 176 \text{ m}^2 \text{ g}^{-1}$) with uniform mesopores (ca. 5.8 nm in diameter). Interestingly, a partial substitution of N and C for O is attained in STO lattice with this synthetic protocol, according to the elemental analysis, and infrared (IR) and X-ray photoelectron spectroscopy (XPS) studies. Compared to STO:C,N, the STO:C,N mesoporous decorated with Pt nanoparticles (ca. 3 nm) present unique attributes that allow for an impressive improvement of up to 74-fold in photocatalytic H₂-production activity. By combining UV-vis/NIR optical absorption, photoluminescence, Raman and electrochemical impedance spectroscopy, we show that this improved performance arises from the unique nanostructure, which provides massive surface active sites, and the proper alignment of defect states and conduction band-edge position of the STO:C,N semiconductor with respect to the interband transitions of metal, which permit efficient plasmon-induced interfacial electron transfer between the Pt-STO:C,N junction.

1. Introduction

Exploiting solar-to-chemical energy conversion by semiconductor-based photocatalysis is a promising means for addressing future energy demands. This approach is based on the generation of bound electron-hole pairs (excitons) in a photochemically active material through sunlight absorption. The photogenerated electrons and holes can subsequently participate in redox reactions, such as water splitting and pollutant degradation [1]. To this end, a growing interest in developing highly-active nanostructured semiconductors has evolved in recent years. Among various morphologies, three-dimensional (3D) nanoporous semiconductors are considered as a class of very promising candidates for photocatalysis due to their high accessible surface area, large exposure of active sites and small dimension of the framework

constituents. These characteristics could enable fast mass-transport kinetics and short electron to the surface pathway, suppressing the rapid recombination of photogenerated carriers in the particle core, and thus facilitating a high rate of photocatalytic reactions [2,3].

Over the past years, a large number of semiconductor materials have been investigated to catalyze the generation of molecular hydrogen from water. Among them, strontium titanate (SrTiO₃, STO) is a key player that is still gaining increased attention in the fields of water splitting and CO₂ fixation catalysis [4]. The unique properties of STO stems from its high charge-carrier mobility along the (001) layered structure (TiO₂ slabs), low concentration of defect sites in the crystal lattice, and excellent chemical stability [5,6]. Moreover, the small exciton binding energy of the STO perovskite, as a result of its large dielectric constant ($\epsilon = 300$), has been proposed to play a key role in its

* Corresponding author.

E-mail address: garmatas@materials.uoc.gr (G.S. Armatas).

photocatalytic performance, leading to a large dissociation of excitons. This means that the majority of photoexcited carriers escape initial recombination and are available as free electrons and holes for consecutive redox reactions. However, notwithstanding these advantageous attributes, STO is a wide band gap semiconductor ($E_g = 3.1\text{--}3.3\text{ eV}$) which requires ultraviolet light ($\lambda < 380\text{ nm}$) for operation; it corresponds only to a 3–4% fraction of the solar spectrum. An effective strategy to overcome the intrinsic limitations of STO is to extend its light absorption into the visible region by incorporating metal (like Rh, Cr, Sb) [7,8] or nonmetal (like C, N, F, S, I) [9–11] impurities into the structure. Even though metal doping can narrow the band gap of the material by creating localized midgap d states, it may also form phase impurities acting as recombination centers for photo-generated electron-hole pairs [12]. Consequently, this process might repress the carrier conductivity and therefore, in-turn, deteriorate the photocatalytic performance. On the contrary, non-metal doping has been shown to be more advantageous in this direction. N^{3–} ions, for example, can be partly substituted for oxygen (O^{2–}) in the oxide lattice, introducing localized N 2p levels at 0.3 to 0.5 eV above the valence band maximum (VBM) of STO, and more importantly, without contributing to the electron-hole pair recombination process [13]. Besides, the p electronic states can overlap sufficient with the O 2p orbitals of the semiconductor, narrowing the band gap. Nevertheless, N dopants, which are typically stabilized inside the titanate lattice via an electron transfer from the high-energy Ti³⁺ states to the partially occupied N 2p orbitals [14], are susceptible to N₂ release during the catalytic reactions [15]. Also, implantation with nitrogen is typically associated with the formation of oxygen vacancies into the structure through introducing localized Ti³⁺ 3d states at about 0.5–1 eV below the conduction band minimum (CBM) of STO [16]. These discrete midgap energy levels, however, might lower the reduction potential of the excited electrons for hydrogen evolution or become trapping sites for interband electron–hole relaxations, impairing the effectiveness of doping. Recently, codoping with trivalent rare-earth (La³⁺, Eu³⁺) and Cr³⁺ cations at the Si²⁺ sites has been demonstrated to compensate the formation of oxygen vacancies in STO and improves photocatalytic efficiency [17].

So far, a variety of well-defined STO nanoparticles with a broad range of morphologies, from nanorods to nanowires and to nanocubes, have already been prepared. Synthetic methods to produce these materials include high-temperature solid-state reaction of precursor salts, sol-gel polymerization, and solvothermal treatment [18–20]. To the best of our knowledge, however, none of these nanomaterials are porous, and their surface area is due to the voids between the particles. In order to develop highly efficient photocatalysts, exploring new design strategies based on the critical requirements of well-defined electronic structure and high density of surface active sites is a pressing issue. Here, we report the synthesis of novel STO nanoparticles with a large intrinsic mesoporosity through a facile two-step synthetic method involving a polymer-assisted sol-gel chemical method followed by a low-temperature solvothermal process. We show that the resulting materials consist of nanocuboid particles, which express a large internal surface area available for reaction, while they can be readily n-type doped by carbon and nitrogen substitutions. By combining optical absorption, photoluminescence and electrochemical impedance spectroscopy results, we also provide insight into the photoelectrochemical behaviour of the unmodified and Pt-loaded implanted STO nanoparticles. The results indicate that the effectiveness of our catalyst in enhancing hydrogen production under UV/Vis-light illumination is determined by the efficient separation and migration of photogenerated carriers through the matched energy levels of the midgap states of C,N-codoped STO and interband transitions of Pt nanoparticles.

2. Experimental

2.1. Materials

Polyoxyethylene-*b*-cetyl ether (Brij 58) block copolymer (HO (CH₂CH₂O)₂₀C₁₆H₃₃, M_n ~ 1124), titanium(IV) chloride (99.9%), hexachloroplatinic(IV) acid hydrate (≥ 98%, H₂PtCl₆·xH₂O), ethylenediamine (≥ 99%), acetic acid (≥ 99.5%) and absolute ethanol (99.8%) were purchased from Sigma-Aldrich. Titanium(IV) propoxide (≥ 98%, TPP) was supplied by Merck. Strontium nitrate (> 99%, Sr(NO₃)₂) was purchased from Alfa-Aesar.

2.2. Synthesis of mesoporous STO and STO:C,N nanoparticles

In a typical synthesis, 0.75 g of polyoxyethylene-*b*-cetyl ether (POE (20)-*b*-C16) block copolymer was dissolved in a mixed solvent of ethanol (2 mL), water (1 mL) and HNO₃ (1 M aqueous solution, 0.1 mL). In a separate vial, 0.38 mmol of TiCl₄ and 1.39 mmol of TPP were dissolved in 2.5 mL of anhydrous ethanol at 5 °C, and the as-formed clear solution was slowly added to the block copolymer solution under vigorous stirring. After 5 min of stirring, 1.77 mmol of Sr(NO₃)₂ was added, and the resulting suspension was then further stirred at 5 °C for 1 h. Then, 10 mL of 1 M NaOH solution were added dropwisely to the reaction mixture (within a ~3 h period), and the obtained suspension was transferred to a 50 mL Teflon-lined autoclave and heated at 80 °C for 18 h. Finally, the white product was collected by filtration, washed thoroughly with 1 M acetic acid and water, and dried at 60 °C overnight. The template was removed by calcination in nitrogen for 4 h at 260 °C and then for 3 h at 400 °C, using a heating rate of 0.5 °C min^{–1}. Mesoporous C/N-codoped SrTiO₃ nanoparticles (ut-STO:C,N), obtained as a light gray powder, were also prepared using a similar procedure, but without the addition of the template.

2.3. Photochemical deposition of Pt on STO:C,N

The Pt-loaded STO:C,N nanoparticles were synthesized through a photochemical reduction method. In a typical procedure, 100 mg of as-prepared STO:C,N nanoparticles were dispersed by vigorous stirring in a aqueous solution (10 mL) containing 20% (v/v) of methanol. Then, a nominal amount of H₂PtCl₆ dissolved in water (1 mg mL^{–1}) was added to the above suspension under stirring, and the resulting mixture was purged with argon for 30 min. The reaction mixture was then irradiated under magnetic stirring for 1 h under 300 W Xe lamp at room temperature. The grey products were isolated by filtration, washed with deionized water several times, and dried at 60 °C overnight. Utilizing this method, we were able to produce Pt-decorated STO:C,N materials with 1, 1.5 and 2 wt% of Pt content. For comparison, Pt-decorated STO (Pt/STO) and ut-STO:C,N (ut-Pt/STO:C,N) catalysts with 1.5 wt% Pt loading were also prepared using unmodified STO and untemplated STO:C,N, respectively, as supports. The Pt content in each Pt-loaded catalyst was confirmed by energy dispersive X-ray spectroscopy (EDS).

2.4. Photocatalytic hydrogen evolution

The photocatalytic experiments for hydrogen production were carried out in an air-tight Pyrex glass reactor with a 300 W Xe arc lamp. In a typical experiment, 20 mg of catalyst was dispersed in 50 mL of water/methanol solution (8:2 v/v) under stirring, and the resulting mixture was purged with argon for more than 30 min to completely remove the air. The reaction mixture was then irradiated under magnetic stirring at 20 °C, using a cooling water system. The evolved gas was analyzed using a gas chromatograph (Shimadzu GC-2014) equipped with a thermal conductivity detector (TCD).

2.5. Physical characterization

Thermogravimetric (TG) analysis was performed using a Perkin-Elmer Diamond system. Thermal analysis was conducted at a heating rate of $5\text{ }^{\circ}\text{C min}^{-1}$ from 40 to $600\text{ }^{\circ}\text{C}$ in air atmosphere (under a $\sim 200\text{ mL min}^{-1}$ flow rate). Small-angle X-ray scattering (SAXS) measurements were performed on a Xenocs Nano-inXider system using $\text{Cu K}\alpha$ radiation ($\lambda = 1.54189\text{ \AA}$). Scattering data were corrected for dark current and empty tube scattering. X-ray diffraction (XRD) patterns of as-prepared samples were collected using a PANalytical X'pert Pro X-ray diffractometer with a $\text{Cu-K}\alpha$ radiation source ($\lambda = 1.5418\text{ \AA}$) at 45 kV and 40 mA, in the Bragg–Brentano geometry. Scanning electron microscope (SEM) images were obtained using a field emission JEOL JSM 7000 F electron microscope operating at 15 kV accelerated voltage. Samples were prepared by depositing a dilute ethanol dispersion of the STO:C,N material onto a glass slide and allowing it to dry under reduced pressure. Energy-dispersive X-ray spectroscopy (EDS) was performed in a JEOL JSM-6390LV SEM instrument operated at 15 kV and equipped with an Oxford INCA PentaFETx3 detector (Oxfordshire, UK). Data acquisition for EDS analysis was performed at least four times for each sample using an accelerating voltage of 20 kV and a 100-s accumulation time. Transmission electron microscopy (TEM) images were recorded with a JEOL JEM-2100 electron microscope (LaB₆ filament) operating at an accelerated voltage of 200 kV. Samples were prepared by dispersing fine powders in ethanol using sonication, followed by depositing a drop of solution onto the carbon-coated Cu grid and evaporating the solvent in air. X-ray photoelectron spectroscopy (XPS) was performed on an ESCALAB photoelectron spectrometer using a monochromatic Al $\text{K}\alpha$ X-ray source ($h\nu = 1486.6\text{ eV}$). All binding energies were referenced to the C 1 s peak (284.8 eV). The atomic concentration of an element (C_i) was determined by the XPS spectra according to the equation $C_i = (A_i/s_i)/\sum_i (A_i/s_i)$, where A_i is the peak area and s_i is the sensitivity factor. Nitrogen adsorption and desorption isotherms were measured at $-196\text{ }^{\circ}\text{C}$ with a Quantachrome NOVA 3200e volumetric analyzer. Before analysis, the samples were degassed at $120\text{ }^{\circ}\text{C}$ under vacuum ($< 10^{-4}\text{ mbar}$) for 12 h. The surface areas were calculated using the Brunauer–Emmett–Teller (BET) model on the adsorption data for 0.05–0.24 relative pressure (P/P_0) region, the total pore volumes were calculated from the adsorbed amount at the P/P_0 of 0.98, and the distributions of pore sizes were derived from the adsorption branch of isotherms, using the non-local density functional theory (NLDFT) method for slit pore geometry. Elemental C, H and N analysis was performed on a Perkin-Elmer 2400 Series II CHNS/O instrument. Raman spectra were collected on a Nicolet Almega XR micro-Raman spectrometer using a laser line at 473 nm wavelength. Fluorescence spectra were obtained at room temperature on a Lumina Fluorescence spectrometer (Thermo scientific) equipped with a 150 W Xenon lamp. Diffuse reflectance UV-vis/near-IR spectra were obtained on a Perkin-Elmer Lambda 950 optical spectrophotometer in the wavelength range 200–2500 nm. BaSO_4 powder was used as a 100% reflectance standard and base material on which the powder sample was coated. Diffuse reflectance data were converted to absorption using the Kubelka-Munk function $\alpha/S = (1-R)^2/(2R)$, where R is the measured reflectance and α, S are the absorption and scattering coefficients, respectively.

2.6. Electrochemical measurements

Mott–Schottky plots were obtained with an electrochemical workstation (CHI 660E). A three-electrode set-up, with a platinum plate ($1.0 \times 2.0\text{ cm}^2$) and a silver–silver chloride (Ag/AgCl, 3 M KCl) as the counter and reference electrodes, respectively, was adopted to study the samples. The capacitance of the semiconductor/electrolyte interface was measured at 1 kHz, with 10 mV AC voltage amplitude in 0.5 M Na_2SO_4 aqueous solution ($\text{pH} = 6.95$). Electrodes for impedance-potential measurements were fabricated as follows: $\sim 10\text{ mg}$ of each

sample was dispersed in 1 mL deionized water, and the mixture was subjected to sonication in a water bath until uniform suspensions were formed. Then, $40\text{ }\mu\text{L}$ of the suspensions were dropped cast onto fluorine-doped tin oxide (FTO, $10\text{ }\Omega\text{ sq}^{-1}$) substrates, which were masked using 3 M scotch tape with an active area of 1 cm^2 . The samples were dried in a $60\text{ }^{\circ}\text{C}$ oven for 30 min. Prior to use, all electrodes were coated with a silicone resin, leaving only the surface of the sample.

For semiconductor-electrolyte interface, the capacitance C_{sc} of the space charge region can be described as follows:

$$\frac{1}{C_{\text{sc}}^2} = \frac{2(E - E_{\text{FB}})}{\epsilon\epsilon_0 A^2 e_0 N_D} \quad (1)$$

where, C_{sc} is the space charge capacitance, E is the applied potential, E_{FB} is the flat band potential of the semiconductor, N_D is the donor density of electrode material, ϵ is the relative dielectric constant (300 for SrTiO_3), ϵ_0 is the permittivity under the vacuum ($8.8542 \times 10^{-10}\text{ F cm}^{-1}$), A is the area of the electrode, and e_0 is the elementary charge ($1.602 \times 10^{-19}\text{ C}$).

The carrier concentration (N_D) of the samples can be calculated using the following equation:

$$N_D = \frac{2(E - E_{\text{FB}}) \cdot C_{\text{sc}}^2}{\epsilon\epsilon_0 e_0} \quad (2)$$

where the term $(E - E_{\text{FB}}) \cdot C_{\text{sc}}^2$ is the reciprocal of the slope of the Mott–Schottky plot.

2.7. Photoelectrochemical measurements

Photoelectrochemical measurements were carried out in a sealed three-electrode cell with the samples as the working electrode (1 cm^2 illumination area), an Ag/AgCl (3 M KCl) as the reference electrode, and a platinum wire as the counter electrode. Photocurrent spectra were acquired in 1 M KOH aqueous electrolyte at a potential of 1 V (vs Ag/AgCl). Before analysis, the electrolyte was purged with N_2 for 30 min to remove the oxygen. Photocurrent curves of sample were measured using a 300 W Xe Arc lamp (model 6258) coupled with a Cornerstone 260 monochromator (model 74125).

3. Results and discussion

3.1. Synthesis and structural analysis of porous STO nanocuboids

Porous nanocuboids of STO were synthesized by a polymer-assisted sol-gel process, followed by solvothermal treatment. In particular, the procedure involves slow sol-gel reaction of $\text{Sr}(\text{NO}_3)_2$, TiCl_4 and titanium(IV) propoxide (TPP) compounds in the presence of polyoxyethylene-*b*-cetyl ether block copolymer (Brij 58, Croda Inc) aggregates in an ethanol/water mixture solution. The mineralization of SrTiO_3 accomplished at $5\text{ }^{\circ}\text{C}$ using an ice bath with gradual addition of 1 M NaOH solution (within a 3 h period). The as-obtained gel product, after being aged for 18 h at $80\text{ }^{\circ}\text{C}$, was gently annealed for 3 h at $400\text{ }^{\circ}\text{C}$ under nitrogen flow to decompose the organic species within the particles and to induce the crystallization of perovskite phase (for details, see Experimental Section). The elimination of the polymer template was confirmed by thermogravimetric (TG) analysis. As shown in Supporting Fig. S1, the TG profile of the mesoporous STO sample shows no appreciable weight loss (ca. 3 wt%) up to $600\text{ }^{\circ}\text{C}$, suggesting successful removal of the template. Interestingly, this procedure can give rise to the formation of porous STO nanostructures co-doped with C and N atoms by using ethylenediamine ($\text{NH}_2(\text{CH}_2)_2\text{NH}_2$) as both carbon and nitrogen source. Under alkaline conditions, the Ti(IV) species are predominantly present as Ti-hydroxo species (usually $[\text{Ti}(\text{OH})_6]^{2-}$ anions derived from TPP and alcoholysis) [21], which readily react with ethylenediamine to give chelate-metal complexes [22]. A light grey colored implantable STO material (STO:C,N) with 2.63% C and 0.18% N content (atomic %) was obtained by adding a stoichiometric

equivalent of ethylenediamine (based on Ti metal concentration) to the reaction mixture. Note that heat treatment has a significant effect on the C and N composition of the prepared materials. For example, annealing the STO:C,N sample to 500 °C in N₂ flow for 3 h led to a remarkable decrease in carbon (0.61 at. %) and nitrogen (0.05 at. %) concentrations. The chemical composition of the template-free STO:C,N materials was determined by elemental C, H and N analysis. In contrast, if the STO sample is prepared without ethylenediamine, a white product with an inconsiderable amount of carbon and nitrogen is obtained; a ca. 0.53% C and no N was detected by elemental analysis. To obtain viable catalysts for H₂ production, a small amount of Pt, i.e., from 1 to 2 wt%, was deposited on the STO:C,N surface by using a straightforward photochemical deposition method (details are available in the Experimental Section). Pt, in particular, has been preferred as a cocatalyst because of its known effectiveness in hydrogen evolution reaction. The Pt content in each Pt/STO:C,N sample was determined by energy-dispersive X-ray spectroscopy (EDS) (on the basis of the Pt/Ti atomic ratio) and was found to be very close to that expected from the stoichiometry of the reactions.

The phase purity and crystal structure of the as-prepared materials were examined by powder X-ray diffraction (XRD). In Fig. 1a, the XRD patterns indicate that the unmodified and C,N-implanted STO samples retain high crystallinity, displaying a series of distinct diffraction peaks, which can be assigned to the cubic close-packed structure of SrTiO₃ with JCPDS no. 74-1296. Notably, no impure phases such as TiO₂ and SrO have been detected by means of XRD. Nevertheless, for Pt-decorated STO:C,N samples, the XRD analysis does not show the crystalline

peaks of Pt, possibly due to the low quantity and small grain size of the Pt nanoparticles (results not shown).

Characterization of the as-made STO:C,N by field-emission scanning electron microscopy (FE-SEM) reveals that this sample is composed of a large number of aggregated cuboid nanoparticles with small diameter (~90–100 nm, see inset of Fig. 1a). In general, the formation process of STO nanoparticles with cubic morphology involves topotactic transformation of titanium oxy-hydroxide (TiO_x(OH)_y) clusters followed by a self-assembly of these secondary units into cuboidal particles through a coalescence and/or Ostwald ripening process [23–25]. It has been demonstrated that for STO perovskite the (100) face has the lowest energy and from a thermodynamic point of view (Wulff construction), the stable morphology of the particles adapts a cube-like shape, which is faceted with (100) planes [26]. The morphology of the implanted STO:C,N nanoparticles was further investigated with transmission electron microscopy (TEM). The TEM images in Fig. 1b–d show individual nanocuboid particles with an edge size of about 100 nm. The diameter of the STO:C,N nanoparticles was also determined by independent small-angle X-ray scattering (SAXS) measurements. As seen in Fig. 1e, analysis of the SAXS data using the indirect transform program GNOM [27] gives a narrow distribution of particle size with an average diameter of ~92 nm, which agrees well with the TEM and FE-SEM images. Meanwhile, SAXS pattern shows a weak but resolved peak at the scattering vector ($q = 4\pi \sin\theta/\lambda$, where 2θ is the scattering angle) of 0.67 nm⁻¹, suggesting mesoscopic order. This scattering vector corresponds to an average repeat distance of ~9.4 nm ($2\pi/q$), which we attribute to the distance between the centers of the pores

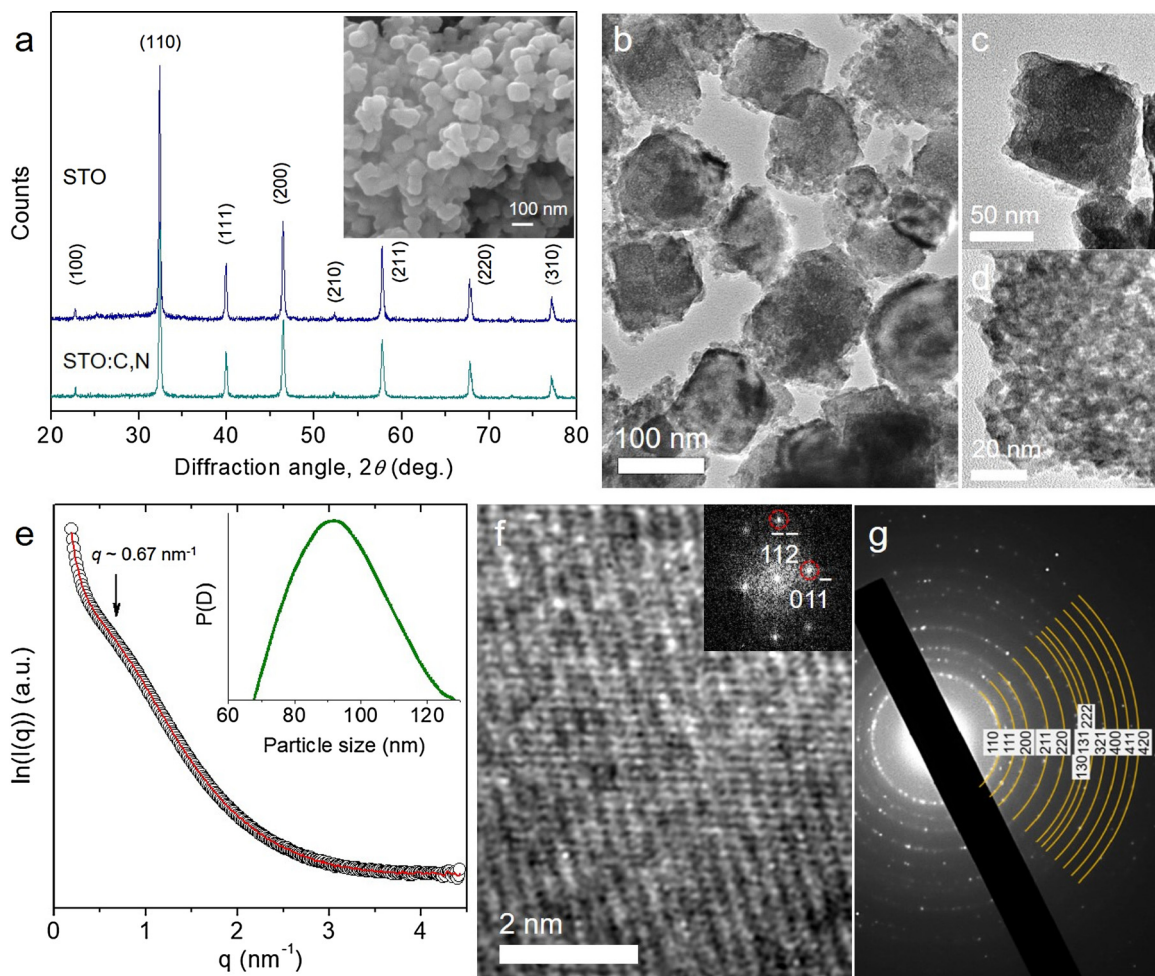


Fig. 1. (a) XRD patterns of mesoporous STO and STO:C,N nanoparticles (Inset: FE-SEM image of STO:C,N), (b) TEM and (c and d) high magnification TEM images, (e) SAXS pattern (Inset: particle size distribution plot derived from scattering data), (f) HRTEM and FFT profile (inset), and (g) SAED pattern of mesoporous STO:C,N.

within the nanoparticles. This implies the formation of a porous structure where the sum of the pore wall thickness and the pore diameter is commensurate with the SAXS repeat distance. Close inspection of the TEM images in Fig. 1c and d reveals that the isolated nanoparticles possess a porous structure within the inorganic framework, in which pores appeared as lighter areas are well-dispersed all over the cuboid nanoparticles. In contrast to other morphologies of STO [7,24,28], the porous architecture of these nanoparticles is a unique feature that is expected to engender more active sites for reactions that can markedly improve the catalytic activity of this system.

A high crystallinity of the nanoparticles is further confirmed by high-resolution TEM (HRTEM) and selected-area electron diffraction (SAED). The HRTEM image taken from a thin area of a particle (Fig. 1f) highlighted the single-crystalline nature of SrTiO_3 . It shows distinct lattice fringes with 1.6 \AA and 2.8 \AA interplanar spacings, which correspond, according to the fast Fourier transform (FFT) pattern (Fig. 1f, inset), to the $(1\bar{1}\bar{2})$ and $(01\bar{1})$ planes (along the $[311]$ direction) of cubic STO, respectively. Furthermore, the SAED pattern in Fig. 1g displays a series of spotted Debye–Scherrer diffraction rings that can be assigned to the perovskite structure of STO, consistent with XRD results. The large number of observed diffraction rings in the SAED pattern corroborates the high crystallinity of the sample. The TEM images of the Pt-loaded catalyst containing 1.5 wt% Pt (hereafter, denoted as Pt/STO:C,N), which is the most effective catalyst of the series, indicated the presence of discrete Pt nanoparticles with a size of about 3 nm on the surface of STO:C,N (see Supporting Fig. S2).

The porosity of the template-free materials was evaluated by nitrogen physisorption at $-196\text{ }^\circ\text{C}$. The analysis showed that all samples exhibit typical type-IV adsorption–desorption isotherms with an H3-type hysteresis loop (Fig. 2a), suggesting the existence of an interconnected mesoporous structure. Besides, the small but defined adsorption step in the mid relative pressure region (0.6 – 0.75 P/P_0) along with the presence of saturation in the adsorption isotherm suggest that the adsorption is due to the mesopore channels within the nanoparticles and not to the interstitial voids between aggregated particles. The Brunauer–Emmett–Teller (BET) surface area and total pore volume of the mesoporous STO and STO:C,N were measured as 176 and $183\text{ m}^2\text{ g}^{-1}$ and $0.31\text{ cm}^3\text{ g}^{-1}$, respectively. Comparatively, after deposition of Pt, the surface area (180 – $182\text{ m}^2\text{ g}^{-1}$) and pore volume (0.20 – $0.30\text{ cm}^3\text{ g}^{-1}$) of the composites were slightly decreased due to the addition of Pt nanoparticles inside the pores (Figs. 2a and S3, Supporting information).

The pore width in these materials was assessed by the adsorption branch of isotherms using the non-local density functional theory (NLDFT) model [29]. The results showed a quite narrow pore-size distribution with an average size of ~ 5.4 – 5.8 nm , see Figs. 2b and S3 (Supporting information). It is worth noting that the untemplated

STO:C,N sample (ut-STO:C,N), which was obtained following a similar procedure as for mesoporous STO:C,N but without template, shows lower porosity (surface area $\sim 146\text{ m}^2\text{ g}^{-1}$ and total pore volume $\sim 0.24\text{ cm}^3\text{ g}^{-1}$, Supporting Fig. S4). Moreover, compared to its templated counterpart, NLDFT analysis on the adsorption data of this material indicates a porous structure with a broader size distribution of pores (average pore size $\sim 7.5\text{ nm}$); these pores presumably arise from interstitial spaces between aggregated particles and small internal (crack) voids in particles due to the liberation (by heating) of ethylenediamine. From the above observations, it appears that the polymer template plays a crucial role in the formation of the mesoporous structure in STO nanoparticles. Table S1 summarises the textural properties of all materials.

Significantly, the C and N atoms are incorporated into the lattice of STO and do not deposit on the surface of the particles. This is particularly important for photocatalysis since incorporation of C and N substituents into STO can induce midgap states between the band edge levels, reducing the band gap and, thus, broadening the light absorption. The implantation of C and N atoms in the STO structure was confirmed by X-ray photoelectron spectroscopy (XPS). Fig. 3a displays a typical high-resolution XPS spectrum of N 1s for the STO:C,N. After deconvolution, two peaks centered at binding energies of 398.7 and 401.7 eV were observed, which can be assigned to the O–Ti–N linkages [30] and surface adsorbed nitrogen species (e.g., NO, NO_2 or NH_x complexes) [31], respectively. This suggests that oxygen is partially substituted by nitrogen, while some nitrogen atoms may also be incorporated interstitially (probably bound to the lattice oxygen) in the oxide lattice. Literature studies suggest that substitutional N dopants contribute to the electronic structure forming impurity levels just above the VBM of STO, while interstitial N atoms do not affect significantly the band states [13]. The incorporation of C and N dopants was further confirmed by the Ti 2p XPS spectrum in Fig. 3b. It shows two Ti 2p doublets with a spin-orbit splitting of about 5.6 eV , corresponding to the $\text{Ti } 2p_{3/2}$ and $\text{Ti } 2p_{1/2}$ core-levels of Ti^{4+} ions (458.3 eV and 463.8 eV) and strong chemical interactions between Ti^{4+} and implanted C/N atoms (461.2 eV and 466.8 eV), respectively [32]. Notably, no $\text{Ti } 2p_{3/2}$ XPS peak was detected in the 455 – 457 eV range, reflecting the absence of reduced Ti^{3+} species in the material. It has reported that N-substitutional electronic states in titania lattice can serve as electron acceptors, promoting the oxidation of Ti^{3+} to Ti^{4+} [33]. We believe a similar explanation may apply here to the XPS results of STO:C,N, that is, an internal electron transfer from the higher energy Ti^{3+} 3d states to the empty N interstitial electronic states. For the C 1s XPS spectrum (Fig. 3b, inset), it can be resolved into three peaks at about 283.6 , 284.8 and 287.2 eV binding energies. The peak at 284.8 eV is attributed to external hydrocarbon impurities, while the peaks at 283.6 and 287.2 eV can be related to the O–Ti–C and C–O linkage, respectively [34,35].

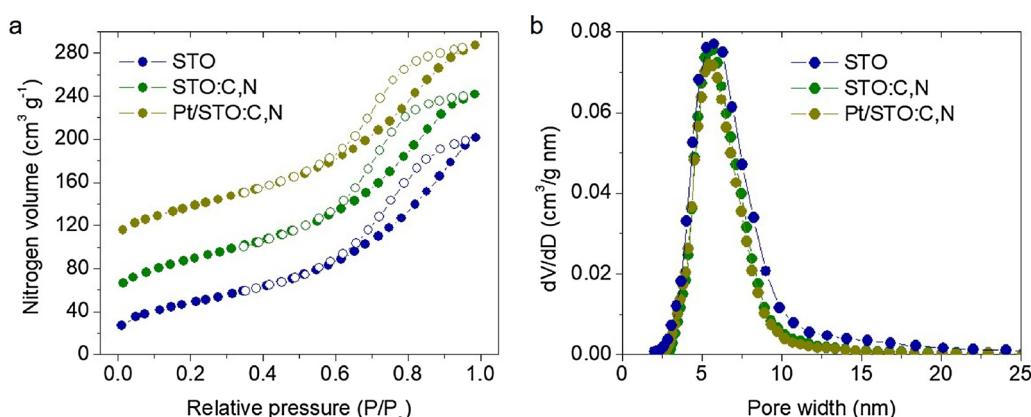


Fig. 2. (a) N_2 adsorption–desorption isotherms at $-196\text{ }^\circ\text{C}$ and (b) the corresponding NLDFT pore-size distributions for mesoporous STO, STO:C,N and Pt/STO:C,N catalysts. For clarity, the isotherms of STO:C,N and Pt/STO:C,N are offset by 40 and $90\text{ cm}^3\text{ g}^{-1}$, respectively.

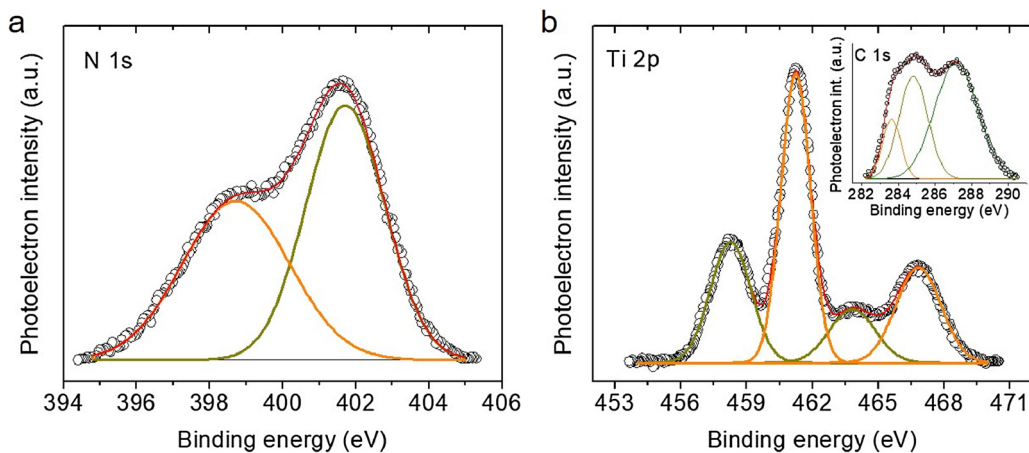


Fig. 3. (a) High-resolution N 1s and (b) Ti 2p_{3/2} and 2p_{1/2} (Inset: C 1s XPS spectrum) XPS spectra of the mesoporous STO:C,N nanoparticles.

This suggests the substitution of some of the lattice oxygen and Ti sites with carbon in STO; although inclusion of interstitial carbonate species (287.2 eV) is a viable possibility. Meanwhile, three peaks at the binding energies of 529.5, 532.4 and 534.9 eV were observed for the O 1s core-levels, which can be assigned, respectively, to the lattice oxygen (Ti–O), surface hydroxyl groups (–OH bonds) and oxygen bound C–O (Supporting Fig. S5) [36]. The C and N atomic concentrations in STO:C,N were also estimated from XPS data and was found to be ~1.82% (based on the 283.6 eV XPS peak) and ~0.15% (based on the 398.7 eV XPS peak), respectively. These results correspond closely to a surface composition of SrTiO_{2.901}C_{0.091}N_{0.008}.

Further evidence for the implantation of C and N into the STO lattice was also obtained by Infrared (IR) spectroscopy. The IR spectrum of STO:C,N in Supporting Fig. S6 shows the characteristic peaks at ~600 cm^{−1} and ~973 cm^{−1} due to the Ti–O–Ti stretching vibration and Sr–O/Ti–O bending vibration (in TiO₆ octahedra) bands of the STO, respectively [37]. Compared to unmodified STO, the STO:C,N exhibits additional peaks at around 1109 and 1198 cm^{−1} that are attributed respectively to the stretching vibration modes of Ti–O–C and C–O bonds. STO:C,N also show weak, yet prominent IR absorption features at ~430 and ~1443 cm^{−1} due to the vibration of interstitial Ti–N and N–O species, respectively [38]. These findings, along with XPS results, further confirm the incorporation of C and N atoms into the strontium titanate matrix (through Ti–O–C/N and Ti–N bonds).

The electronic structure of the STO and STO:C,N mesoporous materials was investigated with optical absorption UV-vis/NIR spectroscopy. In Fig. 4a, the STO displays the characteristic optical absorption near 390 nm, which corresponds to the intrinsic interband transition in

SrTiO₃. Compared to unmodified STO, the UV-vis/NIR spectrum of STO:C,N showed a shift of this absorption edge to longer wavelengths. The red shift in the energy gap for STO:C,N reflects the incorporation of C and N atoms into the STO host matrix, which forms new electronic states with a narrow energy gap at the STO band structure. From the corresponding Tauc plots (Fig. 4a, inset), the optical band gap (E_g) of the mesoporous STO and STO:C,N materials was estimated to be ~3.12 and ~2.97 eV, respectively, using the equation for direct gap semiconductors. Within the UV-vis/NIR absorption region, the STO:C,N also shows an apparently marked tail towards longer wavelengths ($\lambda > 400$ nm), which implies the presence of new midgap states (probably arising from hybridization of the substitutional C 2p and N 2p orbitals with the oxygen ones), in light of previous reports [16,39]. As for the optical absorption spectrum of Pt/STO:C,N showed in Fig. 4a, a noticeable strong absorption in the visible region above 450 nm was observed, which is assigned to the interband (from d band to sp-conduction band) electron transitions in Pt nanoparticles [40].

Fig. 4b shows photoluminescence (PL) emission spectra recorded for the mesoporous STO, STO:C,N and Pt/STO:C,N catalysts under excitation with 280 nm light. PL measurements of the perovskite emission allowed us to gain insights into the transport and recombination dynamics of the photogenerated carriers in the materials. All samples showed an intense PL emission at 379 (3.27 eV) which is related to the photon-assisted band-to-band optical transitions, that is, recombination of free electrons and holes coupled with a low energy (25–50 meV) phonon emission and absorption [41]. In addition, strong PL signals were seen at the violet (394 nm) and blue (450 nm and 465 nm) region that related to shallow (defect levels) and deep intergap states in STO,

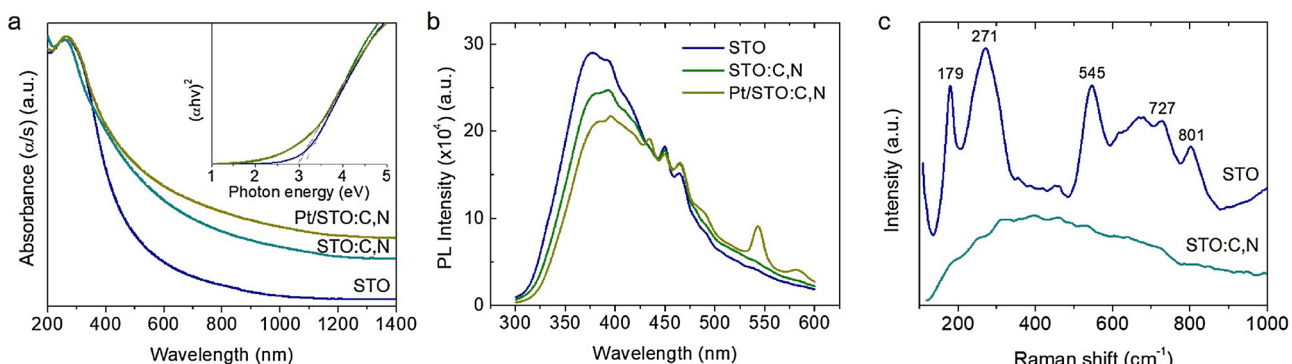


Fig. 4. (a) Optical absorption (Inset: the corresponding Tauc plots: $(\alpha h\nu)^2$ versus photon energy (hv), where α , h and v are the absorption coefficient, Planck's constant and light frequency, respectively) and (b) Room temperature PL spectra of the mesoporous STO, STO:C,N and Pt/STO:C,N materials. PL measurements were performed in water (0.8 mg mL^{−1}) at an excitation wavelength of 280 nm. (c) Raman spectra of mesoporous STO and STO:C,N nanoparticles. (For interpretation of the references to colour in the figure text, the reader is referred to the web version of this article.)

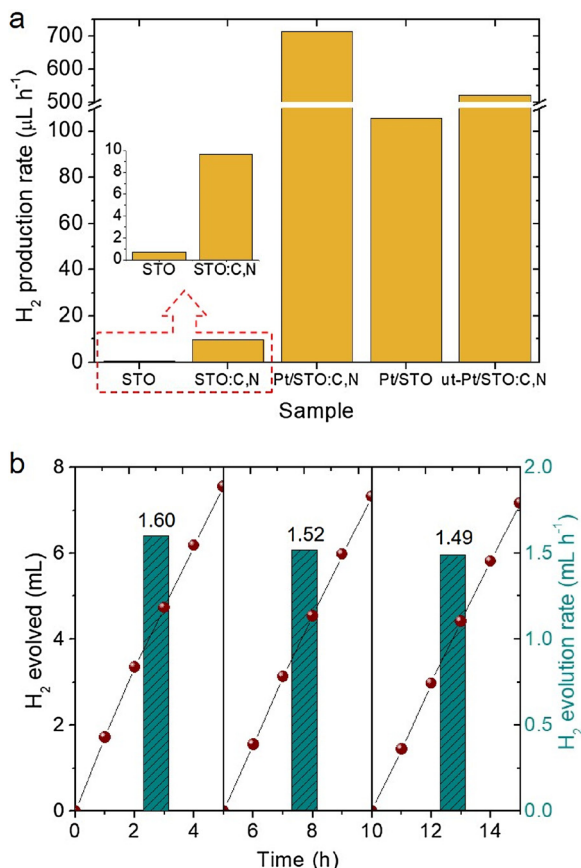


Fig. 5. (a) Photocatalytic H_2 evolution rates for mesoporous STO, STO:C,N, Pt/STO and Pt/STO:C,N nanoparticles and untemplated Pt/STO:C,N (ut-Pt/STO:C,N) sample. (b) Cycling study of the Pt/STO:C,N catalyst. Reaction conditions: 20 mg catalyst (or 0.8 g L^{-1} for stability tests), 50 mL water/methanol mixture (8:2, v/v), UV/Vis-light irradiation ($\lambda \geq 360 \text{ nm}$), 20 °C.

respectively [42]. This suggests that shallow localized electronic states and self-trapped exciton (STE) states exist near the conduction band edge and oxygen vacancies of STO, which may act as carrier traps. It was suggested that electron transitions from defect states (oxygen vacancies) to the top of the valence band or STE states are responsible for photon emission with low energy in oxygen-deficient STO [43]. Comparing with that of STO, PL results of STO:C,N show a noticeable decrease and red-shift (by $\sim 5\text{--}6 \text{ nm}$) of the band-edge and STE emissions, reflecting a lower concentration of defect sites. Moreover, the intense emission of STO:C,N deep-level defects should concern the band edge free excitons, which probably recombine via a trap-assisted radiative pathway, most possibly, by the Shockley-Read-Hall (SRH) recombination mechanism [44]. For Pt/STO:C,N, the quenching of the band-edge (385 nm) and violet (395 nm) emissions entails an efficient interfacial electron transfer along the Pt-STO:C,N junction. Hence the incorporation of Pt nanoparticles appears to mitigate to a significant extent the radiative recombination of excitons through an effective delocalization of charge carriers over the Pt/STO:C,N heterostructure. On the contrary, the intense radiative emission from the intrinsic trap states (peaks at 450, 465 and 490 nm) of Pt-loaded sample suggests that these intergap states may be directly involved in a hot electron transfer from Pt nanoparticles to the semiconductor, probably by Pt interband transitions (see below). The additional blue-green emission bands at $\sim 434 \text{ nm}$ and $\sim 543 \text{ nm}$ appeared after Pt deposition are ascribed to the interband transitions of Pt nanoparticles [45].

For SrTiO_3 with indirect band gap absorption, optical transitions might be mediated by lattice defects or impurities [46]. It was suggested that local distortions in the crystal structure of strontium titanate

due to the stretching of Ti–O bonds (e.g., by Ti displacement) or intrinsic defects (oxygen vacancies) could generate midgap states within the forbidden band of the perovskite; these states might participate in electron relaxation processes [47]. Moreover, the defect sites in STO play a crucial role in affecting the recombination yield of photo-generated carriers and, thus, the photocatalytic activity. We further verified that defects associated with oxygen vacancies or lattice distortions were indeed presented into the STO structure by using Raman spectroscopy. In general, Raman spectroscopy is a useful tool for obtaining valuable information about the local structure (distortions and lattice defects) of the perovskite materials. For unmodified STO with a cubic structure ($Pm3m$ space group), first-order Raman modes are symmetrically forbidden due to the photon moment selection rules [48] and, therefore, such vibrations are weakly observed [49]. Nevertheless, STO Raman modes, especially first-order Raman scattering processes, can be seen when a crystal symmetry breaking takes place due to the presence of long-range electrostatic forces, short distance distortions or oxygen vacancies [25]. Thus, Raman vibrations have been observed in many different defective structures, common in perovskites [50]. Raman spectra for the mesoporous STO and STO:C,N materials in the frequency range of 100–1000 cm^{-1} are illustrated in Fig. 4c. The results showed that mesoporous STO presents intense vibrations at ~ 179 and $\sim 545 \text{ cm}^{-1}$ Raman shifts corresponding to the polar TO_2 ($\text{O}-\text{Sr}-\text{O}$ bending) and TO_4 ($\text{Ti}-\text{O}-\text{Ti}$ bending) modes, and a shift at $\sim 270 \text{ cm}^{-1}$ corresponding to the nonpolar TO_3 mode ($\text{O}-\text{Sr}-\text{O}$ bending) of defective SrTiO_3 [51,52]. Further, the vibration bands observed at ~ 727 and $\sim 801 \text{ cm}^{-1}$ are assigned to the transverse (TO) and longitudinal (LO) optical phonon modes of distorted $[\text{TiO}_6]$ octahedral [41]. In sharp contrast, STO:C,N sample does not display any Raman peak, suggesting the formation of a centrosymmetric structure or at least the presence of local distortions of order less than the phonon wavelength. Thus, combined with the results from XPS (indicating absence of Ti^{3+} sites in STO:C,N) and PL measurements, these findings suggest the oxygen vacancies present in STO were partially filled by the implant atoms in STO:C,N. This observation concurs well with a previous study by Lin et al., who showed that, compared to the intrinsic oxygen lattice sites, surface oxygen vacancies in titania nanoparticles are more susceptible for non-metal (H, N, S, I) doping [53].

3.2. Photocatalytic H_2 -production activity

To visualize the impact of C and N dopants and Pt nanoparticles on the photocatalytic performance of STO, the photoactivity of as-obtained materials was evaluated by measuring the UV/Vis-light irradiated reduction of water towards hydrogen production. The photocatalytic hydrogen evolution reaction experiments were conducted in an airtight Pyrex glass cell, using methanol as the sacrificial reagent, and the results are compared in Fig. 5a. It was corroborated that the H_2 -production activity is substantially higher for STO:C,N ($9.6 \mu\text{L h}^{-1}$) than unmodified STO ($0.7 \mu\text{L h}^{-1}$), indicating the prominent impact of C and N dopants on the photocatalytic efficiency. As expected, the photoactivity of STO:C,N is further remarkably improved with deposition of 1.5 wt% Pt, most commonly due to the electron withdrawal effect of the metal. In general, metal nanoparticles, especially those with high work function such as Pt (5.65 eV), have been considered as efficient electron traps, promoting the separation of photogenerated electron-hole pairs. Furthermore, Pt nanoparticles may offer a proton reduction pathway with low overpotential [54]. As depicted in Fig. 5a, under $\lambda > 360 \text{ nm}$ light, the Pt/STO:C,N catalyst affords an H_2 evolution rate of $714.4 \mu\text{L h}^{-1}$ that is a ~ 74 -fold and more than 1020-fold improvement in photocatalytic activity compared with the pristine STO:C,N and unmodified STO samples, respectively. Interestingly, this activity in H_2 production is far superior to that obtained with Pt-loaded STO catalyst ($105.7 \mu\text{L h}^{-1}$, Pt/STO, Fig. 5a), i.e. the material that is prepared by the photodeposition of 1.5 wt% Pt on STO surface. This suggests that the enhanced photoactivity of Pt/STO:C,N mainly arises from the electronic

transitions within the localized intergap states of STO:C,N and charge transfer interactions with metal nanoparticles. To highlight the superiority of the unique porous architecture of our materials, we performed control experiments where a Pt-loaded catalyst was also prepared by photodepositing 1.5 wt% Pt on untemplated STO:C,N support (ut-Pt/STO:C,N). Interestingly, under identical conditions, this catalyst, although possessing a similar composition (~1.52 wt% of Pt with an average diameter of ~4–5 nm, as determined by EDS and TEM analyses, see Supporting Fig. S7) as the mesoporous Pt/STO:C,N, showed a much lower H₂-production rate (521.2 μL h⁻¹, Fig. 5a). Consequently, these results indicate the critical role of the porous structure not only in providing more surface active sites available for reaction but also in facilitating the mass transfer within the STO:C,N nanoparticles, thus improving photocatalytic efficiency.

It should be stressed that the Pt/STO:C,N catalyst composition was optimized by producing a series of Pt-loaded STO:C,N heterostructures with various Pt loadings (1–2 wt%), and evaluating their H₂-production activity under identical conditions. Reference experiments showed that, with increasing Pt content, the H₂ evolution rate raised to a maximum (714.4 μL h⁻¹) at 1.5 wt%, after which it decreased upon further addition of Pt (Supporting Fig. S8). The H₂-production activity in this study was obtained under typical conditions, that is, using 20 mg of catalyst in 50 mL water containing 20% (v/v) methanol. Upon optimization, however, it is possible to achieve an outstanding H₂ evolution rate of ~1656.4 μL h⁻¹ (or ~68 μmol h⁻¹, at 25 °C) by adjusting the concentration of the Pt/STO:C,N catalyst to 0.8 g L⁻¹ (Supporting Fig. S9). We interpreted the catalyst loading-dependence of the H₂-production activity to an enhancement of the light absorption by the catalyst's nanoparticles. In the same context, an excess amount of catalyst (> 1 g L⁻¹) could reduce the photon absorption capability probably due to the light-screening effect of the particles, thereby resulting in a slightly lower photoactivity. To the best of our knowledge, the activity of our catalyst for hydrogen production is one of the highest so far reported for Pt-loaded STO catalysts. A comparison of the photocatalytic H₂-production activities of different STO-based photocatalysts is shown in Table S2. Apart from photocatalytic H₂ evolution reaction, overall water splitting experiments were also performed with Pt/STO:C,N catalyst (20 mg) suspended in neutral water. As shown in Supporting Fig. S10, the Pt/STO:C,N catalyst exhibits a stable photocatalytic H₂ and O₂ evolution during a 3 h irradiation with UV/Vis light. Under these conditions, the evolution rate of H₂ was ~32.9 μL h⁻¹ and that of O₂ ~16.6 μL h⁻¹, which are very close to the 2:1 stoichiometry of the reaction.

The Pt/STO:C,N catalyst exhibited very good stability under the examined conditions. After three photocatalysis cycles during a 15 h test, the Pt/STO:C,N manifests a persistent H₂ evolution rate of 1.49 mL h⁻¹, which corresponds to the 93% of its initial performance (Fig. 5b). After each testing cycle, the reaction cell was purged with argon until no traces of H₂ and O₂ could be detected by GC analysis. Furthermore, X-ray microanalysis and N₂ physisorption measurements showed no apparent differences in chemical composition and porous structure of the reused sample. EDS results showed a ~1.48 wt% of Pt, while N₂ adsorption data indicated a BET surface area of ~178 m² g⁻¹, pore volume of ~0.29 cm³ g⁻¹ and pore size of ~5.5 nm (Supporting Fig. S11), which are similar to those of the fresh sample. Also, no CO₂ or N₂ gas was detected in the reaction cell by GC, suggesting that Pt/STO:C,N is stable and did not decompose during the photocatalytic reaction.

3.3. Synergistic effect of dopants and Pt nanoparticles on photoactivity

In order to understand the synergistic catalytic activity of dopant atoms and Pt nanoparticles for H₂ evolution, the electrochemical properties of as-prepared materials were investigated with electrochemical impedance spectroscopy (EIS) in the presence of 0.5 M Na₂SO₄ at pH = 7. Fig. 6a displays the Mott-Schottky plots and the

corresponding linear fits of the inverse squares of space-charge capacitance per unit area ($1/C_{sc}^2$) data against the electrochemical potential (E) for the fabricated STO, STO:C,N and Pt/STO:C,N thin-film electrodes. The results show that the flat-band potential (E_{FB}) of STO shifts to a cathodic direction, that is, from -1.02 V to -1.20 V versus the normal hydrogen electrode (NHE) at pH = 7, as the C and N atoms are substituted into the STO lattice. Moreover, the donor (electron) density (N_d) of STO increases upon C and N doping, as evidenced by the change in slope of the $1/C_{sc}^2$ – E curves. By the analysis of the Mott-Schottky plots of STO and STO:C,N samples we found that the electron density is 3.30×10^{15} and 4.06×10^{15} cm⁻³, respectively. Meanwhile, the positive slopes of the linear fits indicate the n-type behaviour of the materials. The observed up-shift in E_{FB} position and increase in N_d concentration for STO upon C and N doping can be explained by considering the formation of Ti-C and Ti-N bonds in implanted STO:C,N sample. Namely, the excess electrons left in the crystal structure, by the substitution of oxygen with C and N atoms, are possibly delocalized among neighboring Ti ions, increasing their electron density and resulting in the formation of localized donor states near the CBM. Moreover, an increase of the electron density on Ti 3d orbitals is anticipated to take place because of the smaller electronegativity of the C and N dopants than that of O atom. Indeed, the presence of these localized donor states will shift the Fermi level upward, improving the n-type conductivity of STO. On the other hand, doping with nitrogen may also create N 2p states above the VBM of STO, pushing the VBM edge to a higher energy and reducing the band gap. This is in line with the red-shifted optical absorption in the UV-vis/NIR spectra (Fig. 4a). When Pt is deposited onto the STO:C,N, E_{FB} moves to more reducing potentials (-1.31 V vs NHE, pH = 7) and donor density gets larger (1.03×10^{16} cm⁻³). This behaviour, although unexpected, could be related to a steeper band bending induced near the metal/semiconductor junction (Schottky depletion), which decrease the thermal relaxation of electrons to lower energy states and improves the carrier separation and transportation within the perovskite. Moreover, a hot electron transfer process, that is, excited electrons from intraband (s-sp) or interband (d-sp) transitions of Pt with sufficient energy to overcome the metal/semiconductor Schottky energy barrier (ϕ_{SBH}) or tunnel through it could be transferred to the semiconductor conduction band (see below).

To investigate possible hot electron transfer processes, the Pt/STO:C,N (1.5% Pt loading) was analyzed by wavelength-dependent photocurrent measurements in 0.5 M KOH with a bias voltage of 1 V. For comparison, STO:C,N and Pt-free and Pt-loaded unmodified STO were also tested under similar conditions. Fig. 6b shows the measured photocurrent signals as a function of the wavelength of incident photons for all the materials under investigation. As expected, STO shows higher photoconductivity when excited with photons of energy ($\lambda < 400$ nm) near the band gap. C,N-implanted STO shows a pretty high photocurrent in the $\lambda < 450$ nm illumination range due to the photon absorption by the defect levels and direct inter-band carrier photoexcitation in STO. Interestingly, Pt/STO:C,N exhibits a broad spectral response of up to 600 nm with photocurrent reaching a maximum at 460 nm, which corresponds to a 4-fold increase relative to the pristine STO:C,N sample. These results evidently reveal that narrowing the bandgap by introducing localized midgap states and incorporating Pt nanoparticles onto the STO is quite effective for enhancing exciton dissociation and charge carrier transfer. The large photocurrent observed for Pt/STO:C,N with wavelengths from 450 to 600 nm, i.e. at energies below the semiconductor's band gap, verifies explicitly the significant role of Pt nanoparticles on the photocurrent enhancement. In particular, this drastic increase in photocurrent could be attributed to the direct electron transfer (DET) from plasmonic Pt to the semiconductor STO:C,N conduction band; comparatively, STO:C,N exhibits a low-to-moderate photocurrent response only below 550 nm. It is well known that semiconductors with high density of states (DOS) in the conduction band, such as STO, can permit efficient hot-electron

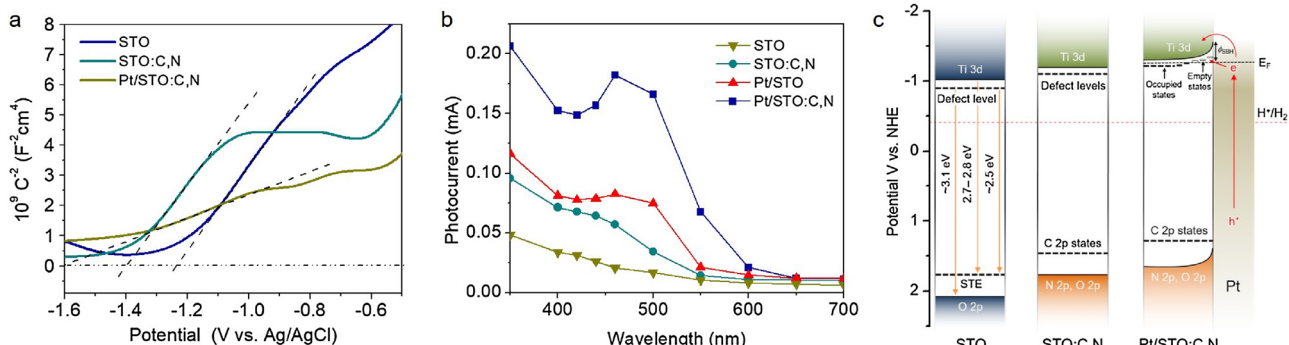


Fig. 6. (a) Mott–Schottky plots (dashed lines are fit to the data), (b) photocurrent curves as a function of different wavelengths measured at a bias of 1 V (vs Ag/AgCl) and (c) energy band structure at the surface (STE: self-trapped exciton states, E_F : Fermi level of the system at the equilibrium, ϕ_{SBH} : Schottky barrier height given by $W_{Pt} - \chi$, where W_{Pt} is the work function of metal and χ is the electron affinity of semiconductor) of the mesoporous STO, STO:C,N and Pt/STO:C,N catalysts. In panel b, the wavelength-dependent photocurrent plot of 1.5% Pt-loaded STO (Pt/STO) sample is also given for comparison. In panel c, a schematic illustration of the band bending of the Schottky junction between Pt and STO:C,N semiconductor is also shown. The VBM energy is estimated from $E_{FB} - E_g$. The valence and conduction band states of STO predominantly consist of O 2p and the Ti 3d orbitals, respectively.

injection [55]. Of course, this process requires good alignment of the Fermi level of the plasmonic nanoparticles with CBM of the semiconductor. Interestingly, the Pt-loaded STO (Pt/STO) material showed a moderately high photoresponse in the 450–600 nm wavelength region, signifying the important contribution of inter-band states of STO:C,N in hot electron transfer process. Complementary, photocurrent measurements at an applied potential of 1 V showed that the Pt/STO:C,N fabricated electrode exhibits much higher photocurrent density ($79.5 \mu\text{A cm}^{-2}$) under 550 nm monochromatic light irradiation when compared to the Pt/STO ($33.0 \mu\text{A cm}^{-2}$), STO:C,N ($26.8 \mu\text{A cm}^{-2}$) and STO ($16.4 \mu\text{A cm}^{-2}$) electrodes. Since Pt nanoparticles mainly absorb light in the 550 nm region due to their distinct characteristic of the interband transitions (as confirmed by UV-vis/NIR and PL spectroscopy), the higher photocurrent in the Pt/STO:C,N is associated with the hot electron transport from the Pt nanoparticles to the STO:C,N semiconductor. Overall, such carrier injection can lead to an increase in the donor (electron) density with a consequently upward shift of the aligned Fermi level and, thus, the CBM of STO:C,N, which is in line with the above EIS and PL results. Also, the up-shift of the Fermi level in STO:C,N can make ϕ_{SBH} smaller, facilitating the smooth hot electron transfer from metal to semiconductor. In light of these results, the lower photoactivity of the Pt/STO:C,N catalyst with 2 wt% Pt content could be tentatively attributed to the higher ϕ_{SBH} due to the increased Pt composition [56]; such an increase in ϕ_{SBH} may suppress the electron transfer process from plasmon-excited Pt to the STO:C,N semiconductor. Although, transfer of plasmonic hot electrons of Au and Ag nanoparticles to the conduction band of a wide gap semiconductor have been reported, even under excitation with low-energy photons (lower than the energy gap of the semiconductor) [57], Pt nanoparticles have rarely investigated. This is the first demonstration of photocatalytic activity over Pt-loaded STO:C,N nanoparticles through charge-transfer from metal to the interfacial electronic states of STO:C,N support. Previously, an electron transfer mechanism from Pt clusters to the TiO₂ substrate was suggested in Pt-loaded TiO₂(110) surface by Sasahara et al., using Kelvin probe force microscope [58]. While more recently, Shiraishi et al., using electron spin resonance (ESR) analysis, have indicated that an electron transfer from Pt particles to anatase is responsible for the visible-light photocatalytic activity of the Pt/TiO₂ system [59].

In the light of the aforementioned findings, we have proposed a charge transfer mechanism for the Pt/STO:C,N catalyst. Fig. 6c shows the band edge energy levels for each catalyst relative to the NHE potential at pH = 7. For highly doped n-type semiconductors, such as STO, the flat-band potential serves as a good approximation of the CBM. Based on this assumption, the VBM can be obtained as the difference between the V_{FB} and energy band gap (E_g) of the samples. Upon

irradiation, the electrons photogenerated in the CBM of STO:C,N are driven from the favorable band-edge positions (Schottky contact) and transfer to the Pt nanoparticles, producing hydrogen. Moreover, an energetic (hot) electron injection from Pt nanoparticles to the defect (acceptor) states and the CBM of STO:C,N due to the heterojunction-driven migration of electrons is also a possible option. Here, in band structure model of Pt/STO:C,N, we assumed an upward band bending of ca. 0.4 eV after contact with Pt nanoparticles [60], while the Fermi level is located almost near the CBM (given an n-type highly doped semiconductor) [61] and the defect states are about 0.1–0.2 eV below the CBM (as inferred by PL spectroscopy) of STO. The defect states, although are occupied by electrons in the bulk region, they are partially empty in the depletion region near the surface, and so become available for accepting photoelectrons (see Fig. 6c). As a consequence, these interfacial charge transfers of the hot electrons (across the Schottky barriers at the Pt–STO:C,N junction) can efficiently suppress the recombination of photogenerated carriers, enhancing the photocurrent responsivity of the catalyst. Simultaneously, the photoexcited holes in the VBM of STO:C,N and in the plasmonic Pt nanoparticles (left due to the hot-electron injection) can transfer to the surface of the catalyst, where they can oxidize methanol. This conclusion is further supported by PL, EIS and wavelength-dependent photocurrent results. Of course, the unique porous heterojunction structure feature between the STO:C,N and Pt nanoparticles, possessing a large surface area and abundant hetero-interfaces, is an advantageous characteristic, as it does favor the transportation of photogenerated electron–hole pairs, contributing to the photocatalytic hydrogen evolution improvement.

4. Conclusions

In summary, we have reported that mesoporous STO nanoparticles can be prepared through a polymer-assisted sol-gel polymerization chemistry. The product comprises a large number of ~ 100 nm-sized nanocuboid particles that possess an inherently large internal surface area (ca. $176 \text{ m}^2 \text{ g}^{-1}$) and demonstrate possibility for doping. The mesoporous implantable STO:C,N nanoparticles at a 1.5 wt% Pt content exhibit a significantly improved photocatalytic H₂ evolution rate of $\sim 68 \mu\text{mol h}^{-1}$, along with a robust stability (up to 15 h irradiation). Moreover, the Pt/STO:C,N catalyst can lead to spontaneous splitting of water to produce hydrogen ($32.9 \mu\text{L h}^{-1}$) and oxygen ($16.6 \mu\text{L h}^{-1}$) under UV/Vis-light irradiation. Our systematic study on the band energy structure of unmodified STO and Pt-free and Pt-loaded STO:C,N nanoparticles revealed that the high photoactivity in the Pt/STO:C,N system arises from the combination effects of enhanced light absorption due to the midgap states and plasmonic scattering effect, efficient hot electron injection, and unique porous nanostructure of the particles.

Given the catalytic importance of the SrTiO_3 , the mesoporous STO:C,N nanoparticles reported may have great implications for environmental remediation and solar energy conversion. Also, the use of plasmonic nanoparticles to absorb and convert visible light of the solar spectrum will widen the range of applications of SrTiO_3 photocatalyst, significantly boosting its overall efficiency.

Acknowledgements

This work was financially supported by the Greek Ministry of Education and the European Union under the ERC grant schemes (ERC-09), University of Crete – Special Account for Research Funds (KA 4121) and Nanyang Technological University under the “Tan Chin Tuan Exchange Fellowship” (FY2016).

Appendix A. Supplementary data

Supplementary material related to this article can be found, in the online version, at doi:<https://doi.org/10.1016/j.apcatb.2018.05.036>.

References

- [1] X.B. Chen, S.H. Shen, L.J. Guo, S.S. Mao, *Chem. Rev.* 110 (2010) 6503.
- [2] I.T. Papadas, I. Vamvasakis, I. Tamiolakis, G.S. Armatas, *Chem. Mater.* 28 (2016) 2886.
- [3] I. Vamvasakis, K.S. Subrahmanyam, M.G. Kanatzidis, G.S. Armatas, *ACS Nano* 9 (2015) 4419.
- [4] Q. Kang, T. Wang, P. Li, L. Liu, K. Chang, M. Li, J. Ye, *Angew. Chem. Int. Ed.* 54 (2015) 841.
- [5] A. Ohtomo, H.Y. Hwang, *Nature* 427 (2004) 423.
- [6] T.K. Townsend, N.D. Browning, F.E. Osterloh, *ACS Nano* 6 (2012) 7420.
- [7] S. Ouyang, H. Tong, N. Umezawa, J. Cao, P. Li, Y. Bi, Y. Zhang, J. Ye, *J. Am. Chem. Soc.* 134 (2012) 1974.
- [8] K. Iwashina, A. Kudo, *J. Am. Chem. Soc.* 133 (2011) 13272.
- [9] Y. Guo, X. Qiu, H. Dong, X. Zhou, *Phys. Chem. Chem. Phys.* 17 (2015) 21611.
- [10] F. Zou, Z. Jiang, X. Qin, Y. Zhao, L. Jiang, J. Zhi, T. Xiao, P.P. Edwards, *Chem. Commun.* 48 (2012) 8514.
- [11] T. Ohno, T. Tsubota, Y. Nakamura, K. Sayama, *Appl. Catal. A* 288 (2005) 74.
- [12] K. Furuhashi, Q. Jia, A. Kudo, H. Onishi, *J. Phys. Chem. C* 117 (2013) 19101.
- [13] Y.Y. Mi, S.J. Wang, J.W. Chai, J.S. Pan, C.H.A. Huan, Y.P. Feng, C.K. Ong, *Appl. Phys. Lett.* 89 (2006) 231922.
- [14] F. Spadavecchia, G. Cappelletti, S. Ardizzone, M. Ceotto, L. Falciola, *J. Phys. Chem. C* 115 (2011) 6381.
- [15] J. Graciani, L.J. Alvarez, J.A. Rodriguez, J.F. Sanz, *J. Phys. Chem. C* 112 (2008) 2624.
- [16] W. Luo, Z. Li, X. Jiang, T. Yu, L. Liu, X. Chen, J. Ye, Z. Zou, *Phys. Chem. Chem. Phys.* 10 (2008) 6717.
- [17] H. Yu, S. Yan, Z. Li, T. Yu, Z. Zou, *Int. J. Hydrogen Energy* 37 (2012) 12120.
- [18] J.Y. Choi, C.H. Kim, D.K. Kim, *J. Am. Ceram. Soc.* 81 (1998) 1353.
- [19] X. Wei, G. Xu, Z.H. Ren, C.X. Xu, W.J. Weng, G. Shen, G.R. Han, *J. Am. Ceram. Soc.* 93 (2010) 1297.
- [20] H. Deng, Y.C. Qiu, S.H. Yang, *J. Mater. Chem.* 19 (2009) 976.
- [21] H. Cheng, J. Ma, Z. Zhao, L. Qi, *Chem. Mater.* 7 (1995) 663.
- [22] L. Hu, J. Wang, J. Zhang, Q. Zhang, Z. Liu, *RSC Adv. A* 4 (2014) 420.
- [23] F. Dang, K. Mimura, K. Kato, H. Imai, S. Wada, H. Haneda, M. Kuwabara, *CrystEngComm* 13 (2011) 3878.
- [24] J.A. Enterkin, K.R. Poeppelmeier, L.D. Marks, *Nano Lett.* 11 (2011) 993.
- [25] A.E. Souza, G.T.A. Santos, B.C. Barra, W.D. Macedo Jr., S.R. Teixeira, C.M. Santos, A.M.O.R. Senos, L. Amaral, E. Longo, *Cryst. Growth Des.* 12 (2012) 5671.
- [26] Q. Kuang, S. Yang, *ACS Appl. Mater. Interfaces* 5 (2013) 3683.
- [27] A.V. Semenyuk, D.I. Svergun, *J. Appl. Crystallogr.* 24 (1991) 537.
- [28] L. Mu, Y. Zhao, A. Li, S. Wang, Z. Wang, J. Yang, Y. Wang, T. Liu, R. Chen, J. Zhu, F. Fan, R. Li, C. Li, *Energy Environ. Sci.* 9 (2016) 2463.
- [29] P.I. Ravikovich, D. Wei, W.T. Chueh, G.L. Haller, A.V. Neimark, *J. Phys. Chem. B* 101 (1997) 3671.
- [30] M. Sathish, B. Viswanathan, R.P. Viswanathan, C.S. Gopinath, *Chem. Mater.* 17 (2005) 6349.
- [31] M. Sathish, B. Viswanathan, R.P. Viswanathan, *Appl. Catal. B: Environ.* 74 (2007) 307.
- [32] U. Sulaeman, S. Yin, T. Sato, *Appl. Catal. B Environ.* 102 (2011) 286.
- [33] M. Batzill, E.H. Morales, U. Diebold, *Phys. Rev. Lett.* 96 (2006) 026103/1.
- [34] Y. Zhang, Z. Zhao, J. Chen, L. Cheng, J. Chang, W. Sheng, C. Hu, S. Cao, *Appl. Catal. B: Environ.* 165 (2015) 715.
- [35] C. Cheng, X. Tan, D. Lu, L. Wang, T. Sen, J. Lei, A.M. El-Toni, J. Zhang, F. Zhang, D. Zhao, *Chem. Eur. J.* 21 (2015) 17944.
- [36] R. Jaiswal, J. Bhamra, N. Patel, A. Dashora, D.C. Kothari, A. Miotello, *Appl. Catal. B: Environ.* 333 (2015) 168.
- [37] V. Porokhonskyy, A. Pashkin, V. Bovtun, J. Petzelt, M. Savinov, P. Samoukhina, T. Ostapchuk, J. Pokorny, M. Avdeev, A. Kholkin, P. Vilarinho, *Phys. Rev. B* 69 (2004) 144104.
- [38] S. Sakthivel, M. Janczarek, H. Kisch, *J. Phys. Chem. B* 108 (2004) 19384.
- [39] R. Asahi, T. Morikawa, T. Ohwaki, K. Aoki, Y. Taga, *Science* 293 (2001) 269.
- [40] N.C. Bigall, T. Härtling, M. Klose, P. Simon, L.M. Eng, A. Eychmüller, *Nano Lett.* 8 (2008) 4588.
- [41] Y. Yamada, Y. Kanemitsu, *Phys. Rev.* 82 (2010) 121103.
- [42] D. Kan, T. Terashima, R. Kanda, A. Masuno, K. Tanaka, S. Chu, H. Kan, A. Ishizumi, Y. Kanemitsu, Y. Shimakawa, M. Takano, *Nat. Mater.* 4 (2005) 816.
- [43] E. Grabowska, M. Marchelek, T. Klimeczuk, G. Trykowski, A. Zaleska-Medynska, *J. Mol. Catal. A: Chem.* 423 (2016) 191.
- [44] W. Shockley, W.T. Read, *Phys. Rev.* 87 (1952) 835.
- [45] S.K. Ghosh, M.M. Alam, D. Mandal, *RSC Adv.* 4 (2014) 41886.
- [46] M. Capizzi, A. Frovà, *Phys. Rev. Lett.* 25 (1970) 1298.
- [47] V.M. Longo, A. Figueiredo, A. Laízaro, M.F. Gurgel, M.G.S. Costa, C.O. Paiva-Santos, J.A. Varela, E. Longo, V.R. Mastelaro, F.S. Vicente, A.C. Hernandes, R.W. Franco, *J. Appl. Phys.* 104 (2008) 023515.
- [48] Y.I. Yuzyuk, *Phys. Solid State* 54 (2012) 1026.
- [49] C.T. Lee, M.S. Zhang, Z. Yin, W. Zhu, *J. Mater. Sci.* 40 (2005) 1277.
- [50] F.A. Rabuffetti, H.-S. Kim, J.A. Enterkin, Y. Wang, C.H. Lanier, L.D. Marks, K.R. Poeppelmeier, P.C. Stair, *Chem. Mater.* 20 (2008) 5628.
- [51] M.L. Moreira, V.M. Longo, W. Avansi, M.M. Ferrer, J. Andres, V.R. Mastelaro, J.A. Varela, E. Longo, *J. Phys. Chem. C* 116 (2012) 24792.
- [52] L.F. Da Silva, W. Avansi, J. Andres, C. Ribeiro, M.L. Moreira, E. Longo, V.R. Mastelaro, *Phys. Chem. Chem. Phys.* 15 (2013) 12386.
- [53] T. Lin, C. Yang, Z. Wang, H. Yin, X. Lu, F. Huang, J. Lin, X. Xie, M. Jiang, *Energy Environ. Sci.* 7 (2014) 967.
- [54] N.M. Markovic, B.N. Grgur, P.N. Ross, *J. Phys. Chem. B* 101 (1997) 5405.
- [55] Z. Wang, Z. Zhong, X. Hao, S. Gerhold, B. Stöger, M. Schmid, J. Sánchez-Barriga, A. Varykhalov, C. Franchini, K. Held, U. Diebold, *PNAS* 111 (2014) 3933.
- [56] T. Uchihara, M. Matsumura, A. Yamamoto, H. Tsubomura, *J. Phys. Chem.* 93 (1989) 5870.
- [57] S. Mubeen, G. Hernandez-Sosa, D. Moses, J. Lee, M. Moskovits, *Nano Lett.* 11 (2001) 5548.
- [58] A. Sasahara, C.L. Pang, H. Onishi, *J. Phys. Chem. B* 110 (2006) 13453.
- [59] Y. Shiraishi, D. Tsukamoto, Y. Sugano, A. Shiro, S. Ichikawa, S. Tanaka, T. Hirai, *ACS Catal.* 2 (2012) 1984.
- [60] Y.-W. Chung, W.B. Weissbard, *Phys. Rev. B* 20 (1979) 3456.
- [61] L. Liu, P. Li, B. Adisak, S. Ouyang, N. Umezawa, J. Ye, R. Kodiyath, T. Tanabe, G.V. Ramesh, S. Ueda, H. Abe, *J. Mater. Chem. A* 2 (2014) 9875.